submitted to *Geophys. J. Int.*

Receiver functions using OBS data: Promises and limitations from numerical modelling and examples from the Cascadia Initiative

Pascal Audet

Department of Earth & Environmental Sciences, University of Ottawa, Ottawa, ON, Canada

SUMMARY

The expanding fleet of broadband ocean-bottom seismograph (OBS) stations is facilitating the study of the structure and seismicity of oceanic plates at regional scales. For continental studies, an important tool to characterize continental crust and mantle structure is the analysis of teleseismic P receiver functions. In the oceans, however, receiver functions potentially suffer from several limiting factors that are unique to ocean sites and plate structures. In this study we model receiver functions for a variety of oceanic lithospheric structures to investigate the possibilities and limitations of receiver functions using OBS data. Several potentially contaminating effects are examined, including pressure reverberations from the water column for various ocean-floor depths and the effects of a layer of low-velocity marine sediments. These modelling results indicate that receiver functions from OBS data are difficult to interpret in the presence of marine sediments, but shallow-water sites in subduction zone forearcs may be suitable for constraining various crustal elements around the locked megathrust fault. We propose using a complementary approach based on transfer function modelling combined with a grid search approach that bypasses receiver functions altogether and estimates model properties directly from minimally processed waveforms. Using real data examples from the Cascadia Initiative, we show how receiver and transfer functions can be used to infer seismic properties of the oceanic plate in both shallow (Cascadia forearc) and deep (Juan de Fuca Ridge) ocean settings.

Key words: Receiver functions – OBS data – Modelling – Cascadia Initiative.

1 INTRODUCTION

Recent years have seen a rapid expansion in the development and deployment of broadband ocean-bottom seismograph (OBS) stations, due in part to the large Cascadia Initiative amphibious array on the west coast and offshore of North America that covers the entire oceanic Juan de Fuca plate (Toomey et al., 2014). Being able to record ground motion on the sea floor yields significant benefits in investigations of Earth structure and plate deformation of a large part of the Earth system. Indeed, instrumentation of the ocean floor will likely provide ground truth evidence regarding models of the geological and geophysical processes that form new ocean crust and mantle at mid-ocean ridges (e.g., the MELT experiment, Forsyth et al., 1998) and recycle them at subduction margins (e.g., DONET, Kaneda et al., 2007). An important element in these investigations is our ability to accurately characterize the structures associated with such processes, in particular that of the oceanic crust and lithospheric mantle.

The study of crustal structure on land using scattered teleseismic P waves (aka receiver functions), has a long and rich history of significant achievements that provided some of the clearest images of Earth structures related to various parts of the tectonic system. In particular, receiver functions have been useful in characterising the variations in the thickness and composition of continental crust (Zandt & Ammon, 1995), the geological processes active at subduction zones as the oceanic plate dives underneath a continent or another oceanic plate (e.g. Bostock et al., 2002; Abers et al., 2009; Kim et al., 2014), in continental transform settings (e.g. Ozacar & Zandt, 2009; Porter et al., 2011; Audet, 2015; Frederiksen et al., 2015) as well as the entanglement and geological transformation of crustal material in large collisional settings (e.g., Nábělek et al., 2009). There is much hope that similar outcomes may be achieved from the application of teleseismic scattering principles to the oceanic crust using OBS data (e.g. Janiszewski & Abers, 2015). Knowledge of the seismic properties of the oceanic crust as it evolves from the ridge to the trench are particularly important to validate current models of subduction zone structures that rely on the correspondence between the downgoing low-velocity zone with the subducting oceanic crust (Audet et al., 2010) and delineate the onset of inferred high pore-fluid pressure region around the locked megathrust fault (Audet et al., 2009; Abers et al., 2009; Janiszewski & Abers, 2015). However, there are mul-

tiple complications related to receiver functions using OBS data and in fact very few studies have reported unambiguous results (e.g. Niu et al., 2007; Ball et al., 2014; Brillon et al., 2013; Reeves et al., 2015; Janiszewski & Abers, 2015). Such complications are mainly associated with ocean wave-related noise sources and the reverberating effects of the overlying water column and thin marine sedimentary layers.

Fortunately, the various sources of ocean-related noise appear to affect the waveforms at periods longer ($>$10 s) than those dominating teleseismic P waves, which are in the range 0.1-1 Hz. The sources of noise have been discussed at length in the literature (see, e.g. Webb, 1998; Crawford & Webb, 2000; Webb & Crawford, 2010; Bell et al., 2015). It appears that the main sources of noise differ between deep-water ($>$500 m below sea level; bsl) and shallow-water ($<$500 m bsl) stations. For deep-water stations, long-period tilt and infragravity waves affect vertical seismograms at frequencies below about 0.04 Hz. Compliance effects (pressure variations created by water waves inducing vertical motion) are strongly depth-dependent and affect vertical motions at frequencies $\sim$0.15 Hz for sites that are 50 m bsl, decreasing to 0.05 Hz for sites at a depth of 500 m bsl (Bell et al., 2015). Compliance can be reliably removed from vertical component data using differential pressure gauge data (Webb & Crawford, 2010; Bell et al., 2015).

The upgoing teleseismic wave-field at the sea floor sets off a series of pressure pulses in the overlying water column that interact and interfere with the main crustal arrivals. The pressure signals mainly affect the vertical component and may be largely suppressed by applying a proper correction (Bostock & Tréhu, 2012). Although they are well known (Thorwart & Dahm, 2005), these potentially contaminating signals are currently ignored in OBS receiver function calculation and modelling. In particular, it is important to account for the solid-fluid transmission and reflection coefficients to model the amplitude of wave conversions accurately. Another shortcoming of the receiver function approach for oceanic crustal structure is the violation of the P-wave component as a minimally-biased estimation of the source. This assumption entails that the P-wave impulse response is sparse with maximum energy at zero-lag time. In the presence of a thin layer of sediments, the strong reverberations typically produce high-amplitude oscillations that contam-

inate the early part of the wave train and source-normalized receiver functions can become difficult to interpret in terms of underlying structure.

Another shortcoming is related to the difficulty in performing modal wave decomposition on the ocean floor. In the absence of upgoing wave mode decomposition, the deconvolution of the vertical from the radial component of motion will suffer from a large positive peak near zero-lag time and an associated negative arrival arising from Gibbs effects that may mask wave conversions from the shallow oceanic Moho. Finally, teleseismic P waves resolve structures with wavelength 1-10 km. Since the oceanic crust is between 5-8 km thick, the Moho conversion for stations in the abyssal plains will arrive under one second after the direct P pulse, thus requiring low-noise signals at high frequencies ($\sim$1 Hz). Reverberations originating at the sea-floor interface will arrive later and contain lower frequencies, which may provide better constraints on crustal structure compared to direct conversions.

A recent study by Janiszewski & Abers (2015) illustrates the potential of receiver functions using OBS data from the Cascadia Initiative. The goal of this paper is to simulate receiver functions from broadband recordings on the ocean floor from a range of crustal models to evaluate our capability to interpret the data. The simulations take into account the various effects caused by the water column, layered structure (e.g., sediments, layered accretionary prism), as well as intrinsic limitations of the data (frequency content, etc.). We also outline a complementary method based on the transfer function approach of Frederiksen & Delaney (2015) combined with a grid search approach that bypasses the deconvolution procedure to estimate crustal properties directly from the observed waveforms. Because several of the waveform complications can be modelled accurately, this approach may provide better quantitative constraints on crustal structure compared to imaging using noisy and biased receiver functions. We then use data from two OBS stations from the Cascadia Initiative and calculate receiver and transfer functions to illustrate the possibilities and limitations of the approach to infer oceanic plate structure.

2 RECEIVER FUNCTIONS

Receiver functions are approximations of the Earth's impulse response to body wave excitation and represent the Earth's reflectivity structure on the receiver side. For instance, P waves convert to S waves at seismic discontinuities; P waves reflect off the traction-free surface and convert to S waves, etc. Receiver functions can be used with either P or S wave as the source wavelet. The starting point for receiver function processing is the assumption that the data are related to the impulse response by the convolutional model (linear, time invariant system). In the following, we restrict ourselves to conversions within the vertical plane (defined by vertical and radial orientations) and ignore out-of-plane conversions due to, e.g., dipping interfaces or elastic anisotropy that would give rise to a tangential impulse response. Considering displacement time series of the vertical ($z(t)$) and radial ($r(t)$) components of motion for an incoming teleseismic P wave, the impulse responses can be written in the frequency domain,

$$Z(\omega) = S(\omega)I_Z(\omega) \tag{1}$$

$$R(\omega) = S(\omega)I_R(\omega), \tag{2}$$

where ω is the angular frequency, $Z(\omega)$, $R(\omega)$ and $S(\omega)$ are the Fourier transforms of $z(t)$, $r(t)$ and the source time function $s(t)$, respectively, and $I_Z(\omega)$ and $I_R(\omega)$ are the frequency-domain impulse responses for the vertical ($i_z(t)$) and radial ($i_r(t)$) components, respectively. If we knew $S(\omega)$ perfectly, we could use it to deconvolve the equations and recover both $i_z(t)$ and $i_r(t)$ accurately. Unfortunately, it is practically impossible to obtain a good estimate of $s(t)$ (or $S(\omega)$), and we therefore have to use simplifying assumptions. An approximate impulse response can be obtained for $i_r(t)$ if we consider the vertical component of motion as the source wavelet ($i_z(t) \approx \sum_j \delta(t_j)$) with dominant energy of order $\mathcal{O}(1)$ at $t_0 = 0$ and widely separated spikes with order $\mathcal{O}(\epsilon)$. This assumption is approximately valid for simple structure involving a single deep interface such as the continental Moho, and corresponds to the property of minimum phase (Bostock, 2004). Using this minimum-phase approximation, we can write the receiver function equation as

$$R(\omega) = Z(\omega)\frac{I_R(\omega)}{I_Z(\omega)} \Rightarrow \tilde{I_R}(\omega) \approx \frac{R(\omega)}{Z(\omega)} \tag{3}$$

where the approximate impulse response $\tilde{I_R}$ corresponds to the so-called receiver function, expressed in the frequency domain. In practice, the spectral division is highly unstable due to zeros in the denominator $Z(\omega)$ from uncorrelated noise. Recovering $\tilde{i_r}(t)$ from this procedure is a typical inverse problem for noise minimization (Press et al., 1992). Common approaches to solving this problem include least-squares and the Wiener deconvolution where the denominator is stabilized by a damping parameter or by the pre-event noise spectrum. The time-domain receiver function $\tilde{i_r}(t)$ is then simply obtained by taking the inverse Fourier transform of $\tilde{I_R}(\omega)$.

An important limitation to receiver functions in the vertical-radial ($Z - R$) coordinate system is that the P wave has non-zero incidence and is therefore not completely isolated onto the vertical component, which results in a large pulse at near zero lag-time in the deconvolved radial component. This near zero-lag pulse implies that thin layers near the surface may be poorly resolved due to the dominant energy near zero lag-time and the large negative side lobe arising from Gibbs effects. A more rigorous approach is to isolate the incident P wave using a modal decomposition (Bostock & Tréhu, 2012), which dramatically reduces the near zero-lag pulse and allows shallow structure to be better resolved. On the seafloor, however, modal decomposition is more complicated (Bostock & Tréhu, 2012) and may introduce an additional source of error in the analysis. In fact, due to the poorly constrained near-seafloor structure, modal decomposition may not be desirable. In this work, we will restrict ourselves to the standard $Z - R$ coordinate system, although the method could be easily adapted to handle the modal decomposition.

3 TRANSFER FUNCTIONS

The presence of a thin layer of sediments or an overlying water column results in a Green's functions that is much less sparse and tends to produce large oscillations in the waveforms; it then becomes difficult to untangle the various arrivals due to structural contacts of interest (e.g., Moho) from receiver functions alone, except for a few particular cases. This limits the application of popular moveout-based stacking techniques (e.g., common conversion point or CCP stacks, H-k stacks, etc.) to estimate layer properties. Recently a different approach was proposed that avoids the noisy and biased deconvolution procedure altogether and estimates layer properties directly

from the waveforms (Frederiksen & Delaney, 2015). In particular, we may re-write equation (3) as

$$R(\omega) = Z(\omega)\frac{I_R(\omega)}{I_Z(\omega)} = T_{RZ}(\omega)Z(\omega), \tag{4}$$

where the transfer function $T_{RZ}(\omega)$ is independent of the source time function and depends only on the individual Green's functions. For stacks of isotropic layers, the Green's functions $i_z(t)$ and $i_r(t)$ will be composed of a series of delta functions, from which we need to take the ratio of their respective Fourier transforms. Unlike receiver function deconvolution, however, the denominator of equation (4) is full band and the transfer function is uniquely determined (Frederiksen & Delaney, 2015). For a given layered velocity model, we can therefore calculate $T_{RZ}(\omega)$ and use it to predict the radial component from the observed vertical component.

Since Green's functions can be easily and rapidly calculated for any stack of layers, it is straightforward to perform a grid search over a range of models and minimize a misfit function between observed and predicted radial waveforms. This method is akin to the H-k stacking technique of Zhu & Kanamori (2000) for very simple Earth structure (i.e., isotropic one-layer crust over half-space mantle) and for land stations. In the ocean, the H-k technique would be extremely difficult to implement because the layers are much thinner (thus producing interference between the various arrivals) and because the effect of the water column needs to be removed prior to modelling in some cases. However, unlike the H-k technique, a grid search based on the transfer function approach can deal with any arbitrary velocity model, including a water column and sedimentary layers. Indeed, these various layers can be easily incorporated in the velocity models (provided we have some a priori knowledge of their properties), and their effects can therefore be accurately predicted in the transfer functions. The technique also avoids discretionary weighting of the various direct and reverberated phases used in the stacking and allows to focus on any layer of interest. In addition to a search for thickness and V_P/V_S values, the grid search can focus on any other layer property (e.g., percent anisotropy, trend and plunge of hexagonal symmetry axis, etc.).

The transfer function $T_{RZ}(\omega)$ corresponds to the approximate impulse response $\tilde{I_R}(\omega)$. The equation therefore directly estimates the receiver function equation and can be used to assess the

various effects expected for OBS data, both in deep and shallow water (see following section). To calculate the Green's functions, we use a reflectivity technique for stacks of uniform, isotropic or anisotropic layers separated by sharp, flat interfaces (Kennett, 1983; Thomson, 1996), modified to take into account reverberations from the water column (Bostock & Tréhu, 2012). Velocity gradients can be simulated by a stack of thin layers with seismic properties increasing incrementally. We restrict our attention to isotropic layers in the following section for illustration purposes.

4 SYNTHETIC RECEIVER FUNCTIONS

In this section, we calculate synthetic receiver functions for various oceanic plate and coastal shelf structures (Fig. 1, Tables 1 and 2). In particular, we examine the effects of the overlying water column, the presence of a thin layer of sediments and our ability to resolve a high $P - S$ velocity ratio (V_P/V_S) of oceanic crust in the subduction zone forearc (Fig. 1). In all examples, we fix the density, P- and S-wave velocities and thickness of a layered oceanic crust based on the average crustal structure of Raitt (1963), underlain by a mantle half-space (Table 1). The oceanic crust is composed of a single 2 km thick Layer 2 for simplicity, as well as a 5 km thick Layer 3. Unless specified otherwise (e.g., subducting oceanic crust models), the V_P/V_S of the oceanic crust is set to 1.78 (Christensen, 1978). In all examples, we use a reference slowness of 0.06 s km^{-1}, in the mid range of possible slowness values for teleseismic waves at 30-90° epicentral distance. Receiver functions are obtained by applying a lowpass filter with a corner frequency of 1 Hz to the transfer functions to simulate the bandwidth of P waves.

4.1 Reference model

As a reference for subsequent examples, we first calculate a synthetic receiver function for an OBS station located on a sediment-free oceanic crust in the abyssal plain at a depth of 4000 meters bsl (Fig. 1). The model (labeled M0) is defined in Table 2. Figure (2) shows the synthetic transfer and receiver functions obtained from the i_z and i_r impulse responses. Several phases can be identified. The discontinuity between Layer 2 and 3 produces a set of positive Ps, Pps (or $PpPs$) and negative Pss ($PpSs + PsPs$) arrivals all within the first 2 seconds of the transfer

function. The discontinuity between Layer 3 and the mantle produces a second set of such arrivals between roughly 1 and 4 seconds. The synthetic receiver function smooths out periods of <1 second, and some of these arrivals (Layer 2-3 Pps and Layer 3-mantle Ps; Layer 2-3 Ps) cannot be identified independently. Moreover, due to the large zero-lag amplitude from the spectral ratio, the earliest arrival cannot be distinguished at all. The first water column reverberation arrives at $t = 5.3$ seconds, and does not contaminate the crustal arrivals.

4.2 Effects of the water column

In the previous example, the effects of the water column are not significant since the pressure reverberations arrive late in the P coda. If we consider the acoustic wavespeed c of the water column to be uniform, the arrival times of the pressure reverberations will accumulate delays proportional to the water column thickness h as integer multiples of $\delta t = h\sqrt{1/c^2 - p^2}$, where p is the horizontal slowness. Each pressure pulse will convert some of its energy to the underlying solid medium and generate elastic scattering that may then interfere with the main crustal arrivals. We examine this effect by calculating synthetic receiver functions for stations located at depths of 2000 m and 1000 m bsl (Fig. 1 and Table 2, models M1 and M2, respectively), which may correspond to locations with various distances from the ridge axis, but we keep the crustal structure constant for illustration purposes.

Figures (3) and (4) show the Green's functions and the recovered receiver function for each case. For model M1 with a water depth of 2000 m, the first pressure reverberation arrives at $t = 2.66$ seconds, which is earlier than the Pps and Pss phases from the discontinuity between Layer 3 and mantle. In the receiver function, these signals contaminate the structural signals and introduce artefacts that can be mis-interpreted as structure. For model M2 with a water depth of 1000 m, the water column reverberations arrive well within the structural signals and completely distort the recovered receiver function. Unless these reverberations can be suppressed through wave field decomposition (Bostock & Tréhu, 2012), receiver functions from intermediate-depth OBS stations (depths of $\sim$1000-2000 m) will suffer from these fluid-solid interactions. Furthermore, water-column multiples are not readily apparent on the filtered receiver function traces due to interference

with other crustal arrivals and the effect of filtering (Figs. 3 and 4). It is therefore impossible to unambiguously detect their presence in the receiver functions.

As a final example, we model a receiver function corresponding to an OBS station located on a passive margin at a depth of 150 m bsl (Fig. 5). For this model, we assume a 20 km thick crust with properties corresponding to Layer 3 of the reference model (Fig. 1 and Table 2; model M3). In this case, the water column reverberations are closely spaced in time. Even though they seem to contaminate the transfer function, the lowpass filter efficiently removes the high-frequency noise and the structural signals can be clearly observed (Fig. 5).

4.3 Effects of marine sediments

The oceanic crust is typically covered by a layer of pelagic or terrigenous sediments, especially near the coast and the trench (e.g. Underwood, 2007). For example, sediment thickness on top of the Juan de Fuca plate increases from zero near the ridge to over two kilometers near the trench (Underwood, 2007). Around passive margins, this layer can be thicker than 10 km. These sediments are characterized by very high V_P/V_S producing strong impedance contrasts at the sediment-basement interface. For example, V_P/V_S can be higher than 10 for unconsolidated sediments with more than 60% porosity and a P velocity approximately equal to 1.8 km s^{-1}, and V_P/V_S is $\sim$2-3 for compacted marine sediments with P velocity between 2.5 and 3 km s^{-1} (Hamilton, 1979). Note that near a mid-ocean ridge with no sedimentary cover, the seismic properties of the uppermost oceanic crust may be similar to those of marine sediments due to the high-porosity and low permeability of fractured rocks (Carlson, 2014).

Figure (6) shows an example for a model with the OBS station at 4000 m bsl located on top of a 1.2 km thick sedimentary layer with a P velocity of 2.5 km s^{-1}, V_P/V_S of 2.5, and a density of 2000 kg m^{-3} (Fig. 1 and Table 2; model M4). The layer of low-velocity marine sediments gives rise to a series of high-frequency reverberating oscillations in the impulse responses that dominate the transfer function and contaminate structural signals of interest (Layer 2-3 and Layer 3-mantle discontinuities, Fig. 6). Interestingly, the first water column reverberation appears to produce wave reverberations within the sedimentary layer (Fig. 6**b**; label SR). The high-frequency oscillations

can also be observed for a station located on the shelf of a passive margin at a depth of 150 m, on top of a 400 m thick layer of sediments (Fig. 1 and Table 2; model M5). In this case, the individual Green's functions appear extremely erratic and the transfer function is dominated by a long wave train of very high-frequency spikes that remain in the filtered receiver function (Fig. 7).

4.4 Offshore subduction forearc structure

As final examples, we examine the capability of receiver functions to resolve the possibly high V_P/V_S of the incoming oceanic crust beneath the continental shelf in a subduction zone forearc. This exercise is particularly important since our understanding of earthquake processes across the transition from the locked megathrust to the slow-slip zone hinges on our ability to detect the presence and continuity of a subducting layer of overpressured material, which may control the stability of the megathrust fault.

One main difference to the previous examples is the presence of the highly heterogeneous accreted wedge material. To simplify the analysis, we will consider an OBS station located on the flat portion of the continental shelf at a depth of 150 m bsl and neglect the effect of sediments. We define a 10 km thick layer of wedge/crust material with a density of 2500 kg m^{-3}, and P- and S-wave velocities of 4.5 and 2.5 km s^{-1}, respectively . We fix the density and P-wave velocity of the oceanic crust and consider two different cases for the S-wave velocity (Fig. 1 and Table 2; models M6 and M6*). In the first case, the oceanic crust has a normal V_P/V_S of 1.78 (model M6); in the second case, we fix V_P/V_S to 2.5 (model M6*) (e.g. Audet et al., 2009). Other model parameters remain constant. We note that the effects of dipping interfaces are also ignored in our simulations.

Figure (8) shows the results for the oceanic crust with normal V_P/V_S (model M6). The small impedance contrast between the overlying wedge/crust and oceanic Layer 2 produces an insignificant signal on the receiver function. The other discontinuities do produce significant signal, however, and could potentially be identified on receiver functions. Figure (9) shows the case of high V_P/V_S over the entire oceanic crust (model M6*). Since the S-wave velocity of Layer 2 is smaller than that of the overlying wedge/crust (downward velocity decrease), we see the appearance of a negative Ps pulse preceding the other crustal arrivals. It might therefore be possible to observe

a high V_P/V_S, depending on the velocity of the overlying material. We note however that these arrivals produce low amplitude receiver function signals, even in the case with a high V_P/V_S. The high noise levels observed on OBS data may in fact overwhelm these structural arrivals and hamper our ability to resolve them.

5 REAL DATA EXAMPLES

Results from the previous section exemplify the difficulties that may be encountered when calculating receiver functions using OBS data, even for noise-free data. The various sources of noise present on the seafloor may make it even more difficult to extract clear receiver functions from OBS data. Nevertheless, Janiszewski & Abers (2015) have shown that clear receiver functions can be obtained even in high-noise environments. In this section, we use data from two broadband OBS stations deployed as part of the Cascadia Initiative offshore of western North America (Figure 10**a**). Station FN07A was deployed on the shelf in the forearc of the Cascadia subduction zone during Year 1 (2011-2012), whereas station J39C was deployed near the Juan de Fuca Ridge during Year 3 (2013-2014) (Toomey et al., 2014). We selected only one year of available data to reflect the typical deployment time of OBS stations. We extract three-component waveforms for all events with magnitude M >5.8 in the epicentral distance range 30° to 90°. We calculate the signal-to-noise ratio (SNR) on 0.05-2 Hz filtered vertical component data within 20 second windows on each side of the predicted P-wave arrival time obtained using the iasp91 model (Kennett, 1991), and extract all waveforms with SNR above 8 dB for station FN07A, and 7 dB for station J39C. The lower threshold for station J39C is due to the slightly higher coherence of receiver functions for this station. Horizontal components are first rotated to East and North using the station orientation inferred from Rayleigh wave polarization (Stachnik et al., 2012; Sumy et al., 2015) and then to radial and transverse orientations. We make no correction for compliance or tilt since they affect the waveforms at frequencies lower than 0.1 Hz (Bell et al., 2015).

Using these data, we first compute receiver functions and show how synthetic data from simple velocity models can match the waveforms. Receiver function deconvolution is performed using a modified Wiener filter that uses pre-event noise on both radial and vertical components to capture

the frequency dependence of micro-seismic noise (Audet, 2010). The receiver functions are then filtered between 0.1 to 0.5 Hz (for station FN07A) and 0.1 to 1.5 Hz (for station J39C) and stacked into 10° back-azimuth and 0.002 s/km slowness bins for visual purposes. A higher frequency band is used for station J39C because the receiver functions remain coherent at those frequencies, perhaps due to a quieter seafloor environment. The same data distribution (before binning) is used in the calculation of synthetic receiver functions.

In a second step, we demonstrate how the transfer function approach can be used to estimate single layer properties using data from the same two stations (FN07A and J39C). Data preparation involves bandpass filtering using the same frequency bands as those used in filtering receiver functions, and we keep filtered radial and vertical waveforms within a 40 second window that includes 10 seconds of pre-event noise.

5.1 Cascadia forearc

We first use data for station FN07A deployed at a depth of 154 m bsl to calculate receiver functions using the procedure described above. Figure (10**b**) shows the radial receiver functions sorted by back-azimuth bins for visual purposes. The data appear somewhat noisy, but still contain coherent arrivals across the different traces. The stack of all radial components is plotted on the top panels of Figures (10**b**) and (10**a**).

We model the radial receiver functions using one-dimensional velocity models that include a forearc crust underlain by a two-layer oceanic crust and half-space mantle (Fig. 11**b** and Table 3; models F1 to F4). The misfit between observed and synthetic receiver functions, generated using the same slowness values, is calculated using a root-mean-square (RMS) error, although we only show the stacks in Figure 11**a**. We first calculate synthetic receiver functions for a model where the oceanic crust is overlain by a lower velocity crustal wedge (model F1; Figure 6b in Janiszewski & Abers, 2015). V_P/V_S for wedge and crustal material is constant at 1.9. This model reproduces the first 10 seconds of receiver function data but fails to match later arrivals (RMS of 2.28). The second model imposes a 3 km-thick low-velocity layer with V_P/V_S of 2.1 on top of a uniform oceanic crust, at the base of the wedge (model F2; Figure 6c in Janiszewski & Abers, 2015). This

model is able to reproduce most of the main arrivals within the first 15 seconds of the receiver function stack (RMS of 2.21). In a third attempt (model F3), we specify a 3 km-thick low-velocity Layer 2 with a V_P/V_S of 2.5, similar to results obtained further downdip (Audet et al., 2009), above a 4 km thick Layer 3. The match to the receiver function stack (RMS of 2.29) is not as good compared to that obtained with model F2, but the synthetic stack still contains the main arrivals. All of these models produce a similar RMS misfit, and none of them successfully reproduce the large negative-positive pulses between 13 to 17 seconds that dominate the observed stack. These late arrivals could possibly be due to deeper, un-modelled structure. We attempt to reproduce the late arrivals by specifying a 30 km-thick anisotropic sub-lithospheric mantle layer characterized by 30% anisotropy with a horizontal fast axis oriented at an azimuth of 250°. This model produces a good match with the observed receiver function stack and a lower misfit (RMS of 2.13). Supplementary Figure S1 shows the fit to the transverse component receiver functions. The transverse component data are much noisier than the radial components, but are consistent with the presence of a deep anisotropic layer. Although this model is ad hoc, these results suggest that signals arriving later than $\sim$13 seconds may in fact be due to deeper mantle structure. We note that no attempt was made to optimize the models, however these results show that receiver functions may provide useful constraints on plate structure in shallow water on the continental shelf.

For the transfer function approach, we use models F2 and F3 (Table 3) and search for the thickness (between 1 and 6 km, steps of 0.2 km) and V_P/V_S (between 1.6 and 3.7, steps of 0.05) of the low-velocity layer (Layer 2 for F3) while maintaining other parameters constant. For model F2, we impose a plate interface at 10 km by co-varying the thickness of the overlying wedge and low-velocity layer. For model F3, we impose a total oceanic crust thickness to 6 km by co-varying the thickness of Layer 3 and the low-velocity Layer 2, thus allowing the possibility that the entire oceanic crust may be characterized by low or high V_P/V_S values. Figure (12**a, c**) shows the misfit (variance) between observed and predicted radial components for all model parameters. The RMS for the lowest misfit is 1.1 and 1.3 for models F2 and F3, respectively, showing an excellent fit between the predicted and observed waveforms. Figure (12**b, d**) shows the observed and predicted radial waveforms for the best-fit models. We also determine an error estimate from the F-test

(Silver & Chan, 1988; Walsh et al., 2013; Frederiksen & Delaney, 2015) and use the contour obtained for a 95% confidence interval to provide error bounds on the estimated model parameters. For model F2, the best-fit estimates give a low-velocity layer thickness of 3.0 km (unconstrained) and V_P/V_S of 1.95±0.125, whereas the best-fit estimates for the low-velocity layer obtained using model F3 give 2.3±0.25 km and V_P/V_S of 2.50±0.21, respectively. These values are very close to those selected in the forward modelling exercise that match receiver function data (Table 3).

As a caveat, we did not model effects associated with dipping interfaces that could slightly bias the estimated parameters. Frederiksen et al. (2015) have shown that neglecting the effects associated with dipping structures may reduce the sharpness of the solution and introduce multiple misfit minima. However, at the low dips expected in a shallow subduction zone, these effects are probably not resolvable due to noise and the small amount of high-quality data available.

5.2 Juan de Fuca Ridge

Janiszewski & Abers (2015) showed that stations located near the Juan de Fuca ridge have high SNR for receiver function calculations, which display a number of coherent arrivals. We examine data for station J39C located on the eastern flank of the Co-Axial ridge axis segment (Fig. 10**a**). Figure (10**c**) shows the receiver functions sorted by back-azimuth bins. The data display prominent positive and negative pulses at ∼0.2 and 1.8 seconds followed by less coherent signals with decreasing amplitude.

We first model receiver function data using a 6 km oceanic crust overlying a half-space mantle (Fig. 13**b** and Table 4; model J1). This model generates low-amplitude synthetic receiver functions that do not reproduce the amplitude and timing of the observed data (Fig. 13**a**; RMS of 4.39). Adding a low-velocity layer at the top of the oceanic crust (Fig. reffig:compJ39C**b** and Table 4; model J2) produces a higher amplitude positive pulse near zero-lag time, and a positive-negative pulse between 3 and 4 seconds that provide a slightly better fit to the receiver function data (RMS of 4.31). However the model fails to reproduce the large negative pulse near 2 seconds (see also Fig. 10**c**). To account for this arrival, we specified a model that contains a 15 km-thick high-velocity mantle layer with 4% higher velocities than the underlying mantle (Fig. 13**b** and Table 4;

model J3). This model improves the fit only marginally (RMS of 4.35). In a final model, we modify the high-velocity layer by adding 30% anisotropy with a horizontal fast axis oriented at an azimuth of 100° (Fig. 13**b** and Table 4; model J4) based on the back-azimuth variations of the negative pulses on the observed receiver functions (Fig. 10**c**), as well as evidence from previous studies (Gaherty et al., 2004; Song & Kim, 2011; Audet, 2013). This model reproduces the large negative arrival near 2 seconds and improves the fit to the radial receiver function data between 0 and 5 seconds (RMS of 4.08). Figure S2 shows the fit to the transverse component receiver functions. Once again, the data are much noisier than the radial components and it is difficult to evaluate the fit to the transverse component waveforms. We could not fit the receiver function data using models that include a slow isotropic or anisotropic layer at greater depth beneath the oceanic lithosphere; however, we did not explore the full range of possible models. Based on these simulations, it appears that receiver functions may provide constraints on mantle structure near mid-ocean ridges.

In the transfer function approach for station J39C, we focus on the properties of the anisotropic mantle layer by fixing the seismic velocities of the oceanic crust and underlying mantle to those of model J4 (Table 4), and search for the thickness (5 to 20 km, steps of 1 km) and percent anisotropy (0 to 30%, steps of 2%) of the high-velocity layer. The trend and plunge of the fast axis of hexagonal symmetry are fixed at 100° and 0°, respectively. Figure (14**a**) shows the misfit between the observed and predicted radial components for both parameters, along with the contour for the 95% confidence interval. The best-fit estimates give a layer thickness of 8±3 km and anisotropy of 26±5%. The observed and predicted radial components for the best-fit parameters are shown in Figure (14**b**).

6 DISCUSSION

The simulations of receiver functions presented in this paper highlight the difficulties in identifying signals arising from structural discontinuities using OBS data, even in the absence of noise. In the simplest cases where the OBS station is located in either deep (∼4000 m) or shallow water (∼150 m), the reverberations from the water column do not contaminate the waveforms. For inter-

mediate water depth, these signals interfere with crustal arrivals and cannot be independently identified in receiver function data, thus making receiver function interpretation extremely difficult. In the presence of a layer of low-velocity sediments on the seafloor, receiver functions become highly oscillatory and in some cases completely erratic. This may be the principal reason why receiver functions for intermediate depth OBS stations on the sedimented Juan de Fuca plate are generally unsuccessful (Janiszewski & Abers, 2015). In this paper we only examined relatively simple layered velocity structure. However, some effects that may further complicate interpretation of receiver function signals were left unexplored (e.g., velocity gradients or layer dip). In reality, the short deployment times of typical OBS experiments and the uncertainty in the orientation of horizontal components may limit the range of model parameters that can be resolved robustly. Some of those effects (e.g., dip, anisotropy) produce wave conversions onto the transverse component of motion, which may be used to provide additional constraints in the inversion of receiver function data (see Supplementary Figs. S1 and S2). Another complication that was ignored is related to high-tilt instruments caused by ocean wave-related noise. Removing the tilting effect requires to calculate the transfer function between an optimally oriented horizontal component in the direction of maximum tilt and the vertical component, which is then used to correct the tilt on the vertical component (Bell et al., 2015). Unfortunately, the horizontal components remain biased by tilt, which may then bias the receiver functions. There is currently no practical solution to remove tilt effects completely from all three components of motion, although the use of a trawl-resistant station design appears to mitigate these effects (Janiszewski & Abers, 2015).

The analysis of data from station FN07A in the forearc of Cascadia is encouraging and indicates that it is possible to both calculate high-quality receiver functions and recover layer properties in a high-noise, subduction zone forearc environment using OBS data. The analysis also indicates that results are sensitive to model specifications (e.g., number of layers, trade-off between depth of low-velocity layer and background velocities, etc.). In particular, we find that receiver functions are well matched using a model in which there is a low-velocity layer either at the top of the oceanic crust (i.e., within the accretionary wedge), or forming the upper crustal layer of the downgoing plate. Receiver function simulations also suggest that late arrivals (approximately 13

seconds following the main P arrival) may be due to deep sub-lithospheric anisotropic structure, perhaps coinciding with the sub-slab asthenosphere in this region. Confirming these results will require more careful investigation using additional data and a wider coverage of OBS stations. Nevertheless, the transfer function results suggest that the $\sim$3 km low-velocity layer has high V_P/V_S (2.0 - 2.5) where the plate interface is approximately 10 km deep, around the section of the megathrust found to be locked in geodetic inversions of interseismic GPS data (e.g. Wang et al., 2003; McCaffrey, 2009). Such high V_P/V_S can be explained by pore-fluid pressures near lithostatic values (Audet et al., 2009; Peacock et al., 2011) or by the presence of a thick, high-porosity and low-velocity sedimentary package (Calvert et al., 2011). These results suggest that the plate boundary is weak around the locked part of the megathrust fault, consistent with low values of inferred fault friction from heat flow data, focal mechanisms and critical wedge taper models (e.g. Wang et al., 1995; Wang & He, 1999; Hardebeck, 2015).

The analysis of data from station J39C near the Juan de Fuca Ridge reveals that deep-sea stations may provide high-quality receiver function data characterized by coherent signal at higher frequencies compared to those obtained at stations deployed at shallower depth below sea level, perhaps due to a quieter seafloor environment. The simulations suggest that prominent receiver function signals may be explained by the presence of a $\sim$10-15 km-thick anisotropic uppermost mantle. Although we did not attempt to constrain the orientation of the fast axis of hexagonal symmetry (due to the small amount of data available), we obtain a good fit with a horizontal axis trending at an azimuth of 100°, almost orthogonal to the ridge axis. Transverse component receiver functions are too noisy to provide additional constraints. We also note that, although this model reasonably fits the receiver function data, we did not attempt to explore the full range of possible models and these results are preliminary. Nevertheless, these initial results are consistent with similar findings in the Atlantic (Gaherty et al., 2004) and in the forearc of several subduction zones worldwide (Audet, 2013), and suggest that the anhydrous uppermost mantle of the Juan de Fuca plate may be characterized by strong fabric due to the crystallographic preferred orientation of olivine generated at the spreading ridge (Song & Kim, 2011). If this interpretation is correct, the anisotropic uppermost mantle layer is also present beneath station FN07A, and its signature could

bias the results obtained above for that station. There is indeed an indication in the transverse component data (e.g., between 5 and 10 seconds at back-azimuths between 200° and 250° in Supplementary Figure S1) that such a layer exists beneath station FN07A, but this will need to be investigated in more detail in a future study.

The transfer function approach proposed by Frederiksen & Delaney (2015) and adapted to OBS data may provide the best route to constrain seismic velocity models from teleseismic P-wave scattering data. In particular, this approach avoids dealing with data deconvolution, which can be biased in a high-noise environment, and uses minimally processed waveforms in the inversion as opposed to using data products (i.e., receiver functions). In addition, instead of trying to remove the effects of the water column and those of sediments that contaminate receiver functions, prior information on these layers can be readily included in the velocity models, which allows to focus on other layers of interest. Nevertheless, the calculation and simulation of receiver functions remain useful in building initial velocity models that can be further constrained using the transfer function approach.

In this paper, we focused on using the transfer function approach to estimate properties of a single layer using a grid search method akin to the H-k stacking technique commonly used for land stations. However, the transfer function approach may also be integrated into a directed Monte-Carlo search (Frederiksen et al., 2003) or a trans-dimensional Bayesian inversion where model complexity is driven by the data (Bodin et al., 2012). This flexibility also allows to focus on any layer or interface of interest, including the lithosphere-asthenosphere boundary (Kawakatsu et al., 2009; Olugboji et al., 2013). The method can also be extended to S receiver functions, but the gains are likely to be less important since the pressure reverberations arrive at positive time lags, as opposed to negative lags for the direct S-to-P conversion from solid-solid interfaces (Kawakatsu et al., 2009; Reeves et al., 2015) and do not contaminate the signals as much.

7 CONCLUSION

In this paper, we examine the effects of the water column and marine sedimentary layer on the recovery of teleseismic P receiver functions for oceanic plate structure using synthetic examples.

This exercise reveals that certain combinations of water-depth and sedimentary layer properties allow the identification of arrivals from structural discontinuities; however, in most cases the biasing effects are large enough to hamper direct interpretation of receiver function data. Using real data examples from the Cascadia Initiative, we show how calculated receiver functions can provide useful information on the properties of the subducting oceanic crust in the forearc of Cascadia, whereas those calculated for a station near the Juan de Fuca Ridge may provide constraints on uppermost mantle structure. Finally, we outline the potential of using a transfer function approach, whereby the radial component of motion is directly predicted from the vertical component using a velocity model, which allows the determination of layer properties directly from the data using a grid search without performing deconvolution. These results hold the promise of estimating layer properties from broadband teleseismic data even in the presence of the contaminating effects discussed above.

ACKNOWLEDGEMENTS

Python codes to calculate receiver functions and to perform synthetic receiver function and transfer function modelling are available from the author. These codes make extensive use of the ObsPy package developed by Beyreuther et al. (2010). The author acknowledges careful reviews by W. Geissler and an anonymous reviewer that improved this paper. This work is supported by the Natural Science and Engineering Research Council of Canada.

References

Abers, G. A., MacKenzie, L. S., Rondenay, S., Zhang, Z., Wech, A. G., & Creager, K. C., 2009. Imaging the source region of Cascadia tremor and intermediate-depth earthquakes, *Geology*, **37**, 1119–1122.

Audet, P., 2010. Temporal variations in crustal scattering structure near Parkfield, California, using receiver functions, *Bull. Seism. Soc. Am.*, **100**, 1356–1362.

Audet, P., 2013. Seismic anisotropy of subducting oceanic uppermost mantle from fossil spreading, *Geophys. Res. Lett.*, **40**, 173–177.

Audet, P., 2015. Layered crustal anisotropy around the San Andreas fault near Parkfield, California, *J. Geophys. Res.*, **120**, 3527–3543, doi:10.1002/2014JB011821.

Audet, P., Bostock, M. G., Christensen, N. I., & Peacock, S. M., 2009. Seismic evidence for overpressured subducted oceanic crust and megathrust fault sealing, *Nature*, **457**, 76–78.

Audet, P., Bostock, M. G., Boyarko, D. C., Brudzinski, M. R., & Allen, R. M., 2010. Slab morphology in the Cascadia fore arc and its relation to episodic tremor and slip, *J. Geophys. Res.*, **115**, B00A16.

Ball, J. S., Sheehan, A. F., Stachnik, J. C., Lin, F.-C., & Collins, J. A., 2014. A joint Monte Carlo analysis of seafloor compliance, Rayleigh wave dispersion and receiver functions at ocean bottom seismic stations offshore New Zealand, *Geochem. Geophys. Geosyst.*, **15**, 50515068.

Bell, S. W., Forsyth, D. W., & Ruan, Y., 2015. Removing noise from the vertical component records of ocean-bottom seismometers: Results from year one of the Cascadia Initiative, *Bull. Seism. Soc. Am.*, **105**, 300–313.

Beyreuther, M., Barsch, R., Krischer, L., Megies, T., Behr, Y., & Wassermann, J., 2010. Obspy: A Python toolbox for seismology, *Seism. Res. Lett.*, **81**, 530–533.

Bird, P., 2003. An updated digital model of plate boundaries, *Geochem. Geophys. Geosyst.*, **4**, doi:10.1029/2001GC000252.

Bodin, T., Sambridge, M., Tkalčić, H., Arroucau, P., Gallagher, K., & Rawlinson, N., 2012. Transdimensional inversion of receiver functions and surface wave dispersion, *J. Geophys. Res.*, **117**, B02301.

Bostock, M. G., 2004. Green's functions, source signatures, and the normalization of teleseismic wave fields, *J. Geophys. Res.*, **109**, B03303.

Bostock, M. G. & Tréhu, A. M., 2012. Wave-field decomposition of ocean bottom seismograms, *Bull. Seism. Soc. Am.*, **102**, 1681–1692.

Bostock, M. G., Hyndman, R. D., Rondenay, S., & Peacock, S. M., 2002. An inverted continental Moho and serpentinization of the forearc mantle, *Nature*, **417**, 536–539.

Brillon, C., Cassidy, J. F., & Dosso, S. E., 2013. Onshore/offshore structure of the Juan de Fuca plate in northern Cascadia from bayesian receiver function inversion, *Bull. Seism. Soc. Am.*, **103**,

2914–2920.

Calvert, A. J., Preston, L. A., & Farahbod, A. M., 2011. Sedimentary underplating at the Cascadia mantle-wedge corner revealed by seismic imaging, *Nat. Geosci.*, **4**, 545–548.

Carlson, R. L., 2014. The influence of porosity and crack morphology on seismic velocity and permeability in the upper oceanic crust, *Geochem. Geosys. Geophys.*, **15**, 10–27.

Christensen, N. I., 1978. Ophiolites, seismic velocities and ocean crustal structure, *Tectonophysics*, **47**, 131–157.

Crawford, W. C. & Webb, S. C., 2000. Identifying and removing tilt noise from low-frequency (<0.1 hz) seafloor vertical seismic data, *Bull. Seism. Soc. Am.*, **90**, 952–963.

Forsyth, D. W., Scheirer, D. S., Webb, S. C., Dorman, L. M., Orcutt, J. A., Harding, A. J., Blackman, D. K., Morgan, J. P., Detrick, R. S., Shen, Y., Wolfe, C. J., Canales, J. P., Toomey, D. R., Sheehan, A. F., Solomon, S. C., & Wilcock, W. S. D., 1998. Imaging the deep seismic structure beneath a mid-ocean ridge: The MELT Experiment, *Science*, **280**, 1215–1218.

Frederiksen, A., Folsom, H., & Zandt, G., 2003. Neighborhood inversion of teleseismic *ps* conversions for anisotropy and layer dip, *Geophys. J. Int.*, **155**, 200–212.

Frederiksen, A. W. & Delaney, C., 2015. Deriving crustal properties from the P coda without deconvolution: the southwestern Superior Province, North America, *Geophys. J. Int.*, **201**, 1491–1506.

Frederiksen, A. W., Thompson, D. A., Rost, S., Cornwell, D. G., Gülen, L., Houseman, G. A., Kahraman, M., Poyraz, S. A., Teoman, U. M., Türkelli, N., & Utkucu, M., 2015. Crustal thickness variations and isostatic disequilibrium across the North Anatolian Fault, western Turkey, *Geophys. Res. Lett.*, **42**, doi:10.1002/2014GL062401.

Gaherty, J. B., Lizarralde, D., Collins, J. A., Hirth, G., & Kim, S., 2004. Mantle deformation during slow seafloor spreading constrained by observations of seismic anisotropy in the western Atlantic, *Earth Planet. Sci. Lett.*, **228**, 255–265.

Hamilton, E. L., 1979. v_p/v_s and Poisson's ratios in marine sediments and rocks, *J. Acoust. Soc. Am.*, **66**, 1093–1101.

Hardebeck, J. L., 2015. Stress orientations in subduction zones and the strength of subduction

megathrust faults, *Science*, **349**, 1213–1216.

Janiszewski, H. & Abers, G. A., 2015. Imaging the plate interface in the cascadia seismogenic zone: New constraints from offshore receiver functions, *Seism. Res. Lett.*, **86**, 1261–1269.

Kaneda, Y., Kawaguchi, K., Araki, E., Matsumoto, H., Nakamura, T., Ariyoshi, K., Kamiya, S., Hori, T., & Baba, T., 2007. Dense ocean floor network for mega thrust earthquakes and tsunamis around the Nankai Trough in Southwestern Japan, in *Proc. Int. Conf. on ENVIRONMENT, ECOSYSTEMS and DEVELOPMENT*, pp. 401–404, WSEAS, Tenerife, Spain.

Kawakatsu, H., Kumar, P., Takei, Y., Shinohara, M., Kanazawa, T., Araki, E., & Suyehiro, K., 2009. Seismic evidence for sharp lithosphere-asthenosphere boundaries of oceanic plates, *Science*, **324**, 499–502.

Kennett, B. L., 1983. *Seismic wave propagation in stratified media*, Cambridge University Press, Cambridge, UK.

Kennett, B. L. N., 1991. *IASPEI 1991 seismological tables*, Canberra : Research School of Earth Sciences, Australian National University, On cover: "iasp91".

Kim, Y., Abers, G. A., Li, J., Christensen, D., Calkins, J., , & Rondenay, S., 2014. Alaska Megathrust 2: Imaging the megathrust zone and Yakutat/Pacific plate interface in the Alaska subduction zone, *J. Geophys. Res.*, **119**, 1924–1941.

McCaffrey, R., 2009. Time-dependent inversion of three-component continuous GPS for steady and transient sources in northern Cascadia, *Geophys. Res. Lett.*, **36**, L07304.

Nábělek, J., Hétenyi, G., Vergne, J., Sapkota, S., Kafle, B., Jiang, M., Chen, J., Huang, B.-S., & the Hi-CLIMB team, 2009. Underplating in the Himalaya-Tibet collision zone revealed by the Hi-CLIMB experiment, *Science*, **325**, 1371–1374.

Niu, F., Bravo, T., Pavlis, G., Vernon, F., Rendon, H., Bezada, M., & Levander, A., 2007. Receiver function study of the crustal structure of the southeastern Caribbean plate boundary and Venezuela, *J. Geophys. Res.*, **112**, B11308.

Olugboji, T. M., Karato, S., & Park, J., 2013. Structures of the oceanic lithosphere-asthenosphere boundary: Mineral-physics modeling and seismological signatures, *Geochem. Geophys. Geosyst.*, **14**, 880–901.

Ozacar, A. A. & Zandt, G., 2009. Crustal structure and seismic anisotropy near the San Andreas Fault at Parkfield, California, *Geophys. J. Int.*, **178**, 1098–1104, doi:10.1111/j.1365246X.2009.04198.

Peacock, S. M., Christensen, N. I., Bostock, M. G., & Audet, P., 2011. High pore pressures and porosity at 35 km depth in the Cascadia subduction zone, *Geology*, **39**, 471–474.

Porter, R., Zandt, G., & McQuarrie, N., 2011. Pervasive lower-crustal seismic anisotropy in Southern California: Evidence for underplated schists and active tectonics, *Lithosphere*, **3**, 201–220.

Press, W. H., Teukolsky, S. A., Vetterling, W. T., & Flannery, B. P., 1992. *Numerical Recipes in FORTRAN: The Art of Scientific Computing*, Cambridge Univ. Press, 2nd edn.

Raitt, R. W., 1963. The crustal rocks, in *The Sea*, vol. 3, pp. 85–102, Wiley, New York.

Reeves, Z., Lekić, V., Schmerr, N., Kohler, M., & Weeraratne, D., 2015. Lithospheric structure across the California Continental Borderland from receiver functions, *Geochem. Geophys. Geosyst.*, **16**, 246–266.

Silver, P. G. & Chan, W. W., 1988. Implications for continental structure and evolution from seismic anisotropy, *Nature*, **335**, 34–39.

Song, T.-R. A. & Kim, Y., 2011. Anisotropic uppermost mantle in young subducted slab underplating Central Mexico, *Nat. Geosci.*, **5**, 55–59.

Stachnik, J. C., Sheehan, A. F., Zietlow, D. W., Yang, Z., Collins, J., & Ferris, A., 2012. Determination of New Zealand ocean bottom seismometer orientation via Rayleigh-wave polarization, *Seismol. Res. Lett.*, **83**, 704–712.

Sumy, D. F., Lodewyk, J. A., Woodward, R. L., & Evers, B., 2015. Ocean-bottom seismograph performance during the Cascadia Initiative, *Seism. Res. Lett.*, **86**, 12381246.

Thomson, C. J., 1996. Notes on waves in layered media to accompany program Rmatrix, in *Seismic waves in complex 3-D structures*, pp. 147–162, Department of Geophysics, Charles University.

Thorwart, M. & Dahm, T., 2005. Wavefield decomposition for passive ocean bottom seismological data, *Geophys. J. Int.*, **163**, 611–621.

Toomey, D., A.H.Barclay, R. A., Bell, S., Bromirski, P., Carlson, R., Chen, X., Collins, J., Dziak, R., Evers, B., Forsyth, D., Gerstoff, P., Hooft, E., Livelybrooks, D., Lodewyk, J., Luther, D. S., McGuire, J., Schwartz, S., Tolstoy, M., Théhu, A. M., Weirathmueller, M., & Wilcock, W., 2014. The Cascadia Initiative: A sea change in seismological studies of subduction zones, *Oceanography*, **27**, 138–150.

Underwood, M. B., 2007. Sediment inputs to subduction zones: Why lithostratigraphy and clay mineralogy matter, in *The seismogenic zone of subduction thrust faults*, pp. 42–85, eds Dixon, T. H. & Moore, J. C., Cambridge Univ. Press, Cambridge, UK.

Walsh, E. R., Arnold, R., & Savage, M. K., 2013. Silver and Chan revisited, *J. Geophys. Res.*, **118**, 5500–5515.

Wang, K. & He, J., 1999. Mechanics of low-stress forearcs: Nankai and Cascadia, *J. Geophys. Res.*, **104**, 15191–15205.

Wang, K., Mulder, T., Rogers, G. C., & Hyndman, R. D., 1995. Case for very low coupling stress on the Cascadia subduction fault, *J. Geophys. Res.*, **100**, 12907–12918.

Wang, K., Wells, R., Mazzotti, S., Hyndman, R. D., & Sagiya, T., 2003. A revised dislocation model of interseismic deformation of the Cascadia subduction zone, *J. Geophys. Res.*, **108**, 2026.

Webb, S. C., 1998. Broadband seismology and noise under the ocean, *Rev. Geophys.*, **36**, 105–142.

Webb, S. C. & Crawford, W. C., 2010. Shallow-water broadband OBS seismology, *Bul. Seism. Soc. Am.*, **100**, 1770–1778.

Zandt, G. & Ammon, C. J., 1995. Continental crust composition constrained by measurements of crustal Poisson's ratio, *Nature*, **374**, 152–154.

Zhu, L. & Kanamori, H., 2000. Moho depth variation in southern California from teleseismic receiver functions, *J. Geophys. Res.*, **105**, 2969–2980.

Table 1. Seismic properties of various layers used in the velocity models (Raitt, 1963), with units in parentheses. ρ is density, V_P and V_S are P- and S-wave velocities, respectively.

Layer	ρ (kg m^{-3})	V_P (km s^{-1})	V_S (km s^{-1})
Water	1027	1.5	-
Sediments	2000	2.5	1.0
Wedge	2500	4.5	2.5
Layer 2	2800	5.0	2.8
Layer 2*	2800	5.0	2.0
Layer 3	2800	6.7	3.76
Mantle	3200	8.1	4.55

Table 2. Layer thickness (in km) used in models M0 to M6 described in the text. The lithospheric mantle is defined as a half-space underlying Layer 3.

Layer	M0	M1	M2	M3	M4	M5	M6	M6*
Water	4	2	1	0.15	4	0.15	0.15	0.15
Sediments	-	-	-	-	1.2	0.4	-	-
Wedge	-	-	-	-	-	-	10	10
Layer 2	2	2	2	-	2	-	2	-
Layer 2*	-	-	-	-	-	-	-	2
Layer 3	5	5	5	20	5	20	5	5

Table 3. Velocity models used to generate synthetic receiver functions for station FN07A. H is layer thickness, ρ is density, V_P and V_S are P- and S-wave velocities, respectively. The asterisk indicates a layer characterized by 30% anisotropy with a horizontal fast axis of hexagonal symmetry trending at an azimuth of 250°.

Model	Layer	H (km)	ρ (kg m^{-3})	V_P (km s^{-1})	V_S (km s^{-1})
F1	Wedge	11.0	2500	3.8	2.0
	Layer 2	2.5	2800	6.08	3.2
	Layer 3	3.5	2800	6.65	3.5
	Mantle	-	3200	8.1	4.55
F2	Wedge	6.5	2500	3.8	2.0
	Low-velocity layer	3.0	2800	3.1	1.48
	Oceanic crust	5.0	2800	5.9	3.0
	Mantle	-	3200	8.1	4.55
F3	Wedge	10.0	2500	4.5	2.52
	Layer 2	3.0	2800	4.05	1.62
	Layer 3	4.0	2800	6.0	3.38
	Mantle	-	3200	7.8	4.33
F4	Wedge	10.0	2500	4.5	2.52
	Layer 2	3.0	2800	4.05	1.62
	Layer 3	4.0	2800	6.0	3.38
	Mantle	80	3200	7.8	4.33
	Mantle Lid*	30	3200	7.8	4.33
	Mantle	-	3200	7.8	4.33

Table 4. Velocity models for station J39C. Table format is the same as Table 3. The asterisk indicates a layer characterized by 30% anisotropy with a horizontal fast axis of hexagonal symmetry trending at an azimuth of 100°.

Model	Layer	H (km)	ρ (kg m^{-3})	V_P (km s^{-1})	V_S (km s^{-1})
J1	Crust	6.0	2800	6.0	3.36
	Mantle	-	3200	7.9	4.3
J2	Low-velocity layer	0.3	2800	3.0	1.2
	Crust	6.0	2800	6.0	3.76
	Mantle	-	3200	7.9	4.3
J3	Crust	6.0	2800	6.0	3.76
	High-velocity mantle	15.0	3200	8.2	4.6
	Mantle	-	3200	7.9	4.3
J4	Crust	6.0	2800	6.0	3.76
	High-velocity mantle*	15.0	3200	8.2	4.6
	Mantle	-	3200	7.9	4.3

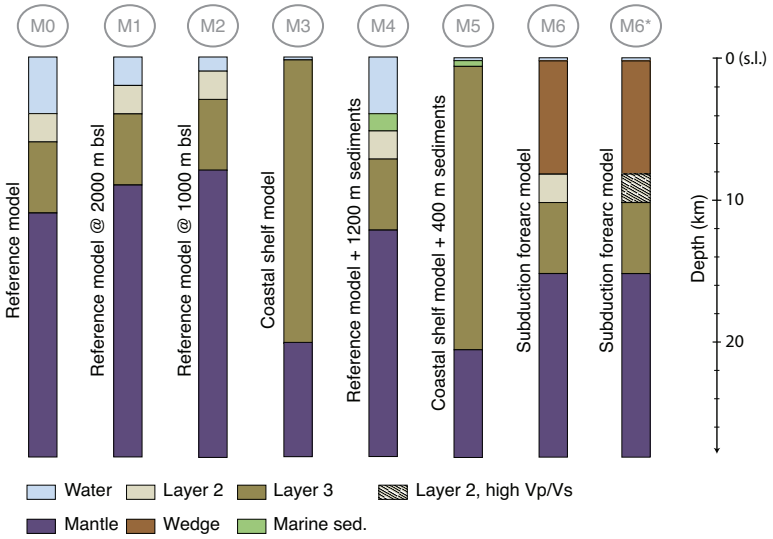

Figure 1. Velocity models considered in the modelling exercise. The reference velocity model (M0) consists of a 2-layer oceanic crust at a depth of 4000 m bsl (shown on the scale to the right). The order from left to right corresponds to the order in which the models M1 to M6 are discussed in the text. Model parameters are listed in Tables (1) and (2) and in the text.

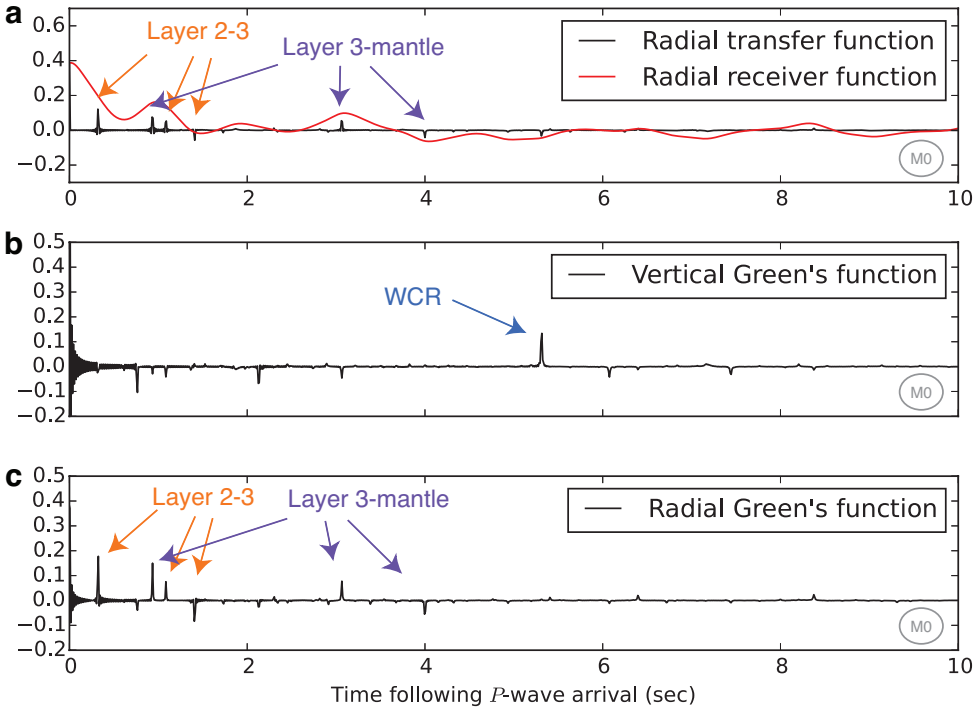

Figure 2. a, Results of transfer function (black) and synthetic receiver function (red) obtained from the vertical (**b**) and radial (**c**) Green's functions calculated for the reference velocity model (M0, Fig. 1) at a OBS station located in the abyssal plain at 4000 m bsl. Various discrete phase arrivals are identified. WCR: water column reverberations; Layer 2-3: intra-crustal discontinuity; Layer 3-mantle: crust-mantle discontinuity. In this and all following examples, we use a back-azimuth of 0° and a slowness of 0.06 s km^{-1}.

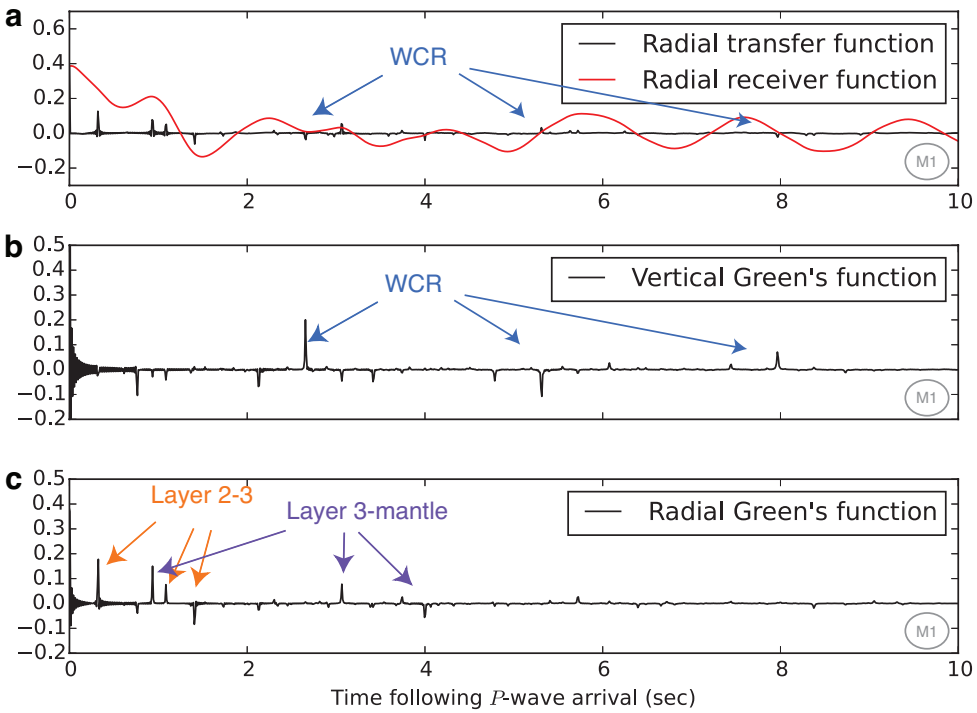

Figure 3. Results for an OBS station located at a depth of 2000 m bsl (model M1, Fig. 1). In this example the water-column reverberations start to contaminate the recovered receiver function and introduce large artificial oscillations at $t > 5$ seconds. Figure format is the same as Figure (2).

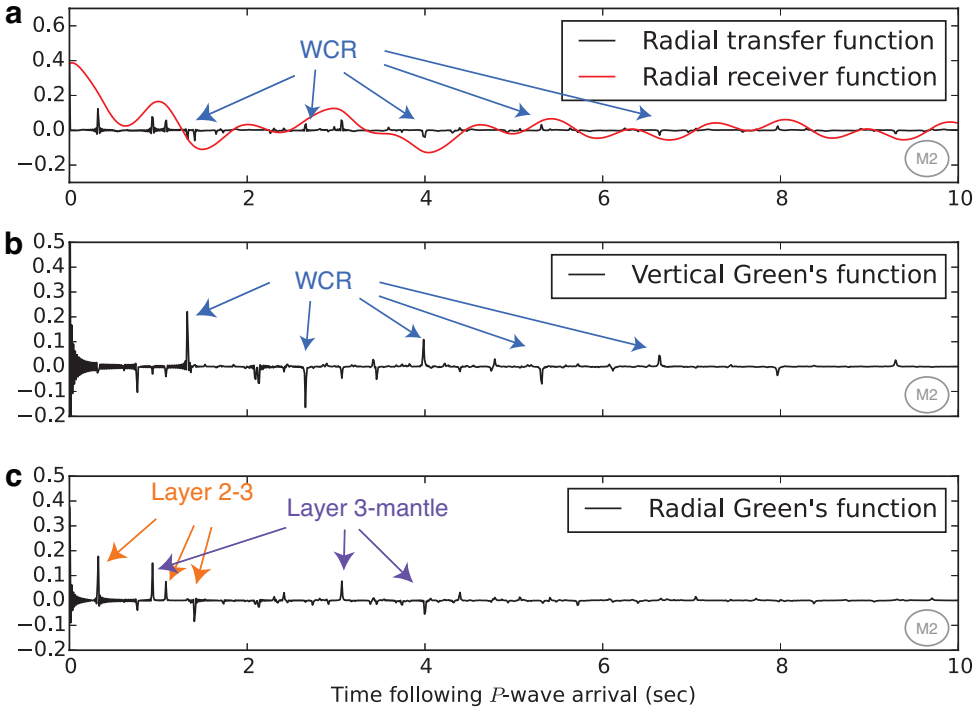

Figure 4. Results for an OBS station located at a depth of 1000 m bsl (model M2, Fig. 1). In this case the water-column reverberations strongly contaminate the recovered receiver function and introduce artificial oscillations at $t > 5$ seconds. Figure format is the same as Figure (2).

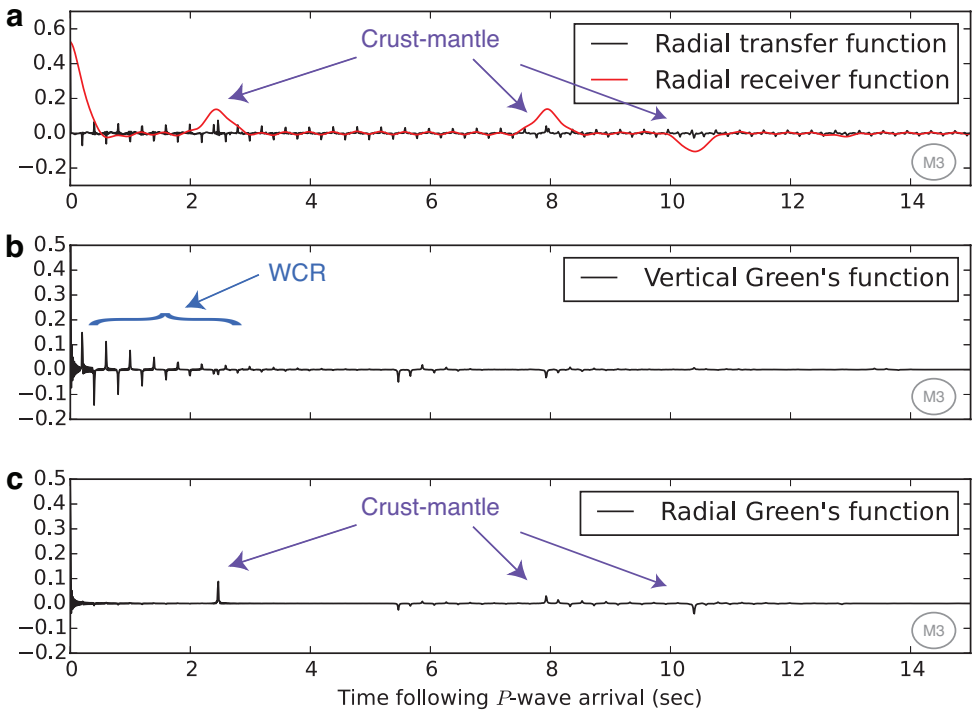

Figure 5. Results for the continental shelf model for an OBS station located at a depth of 150 m bsl on a 20 km thick crust (model M3, Fig. 1; Table 1). In this case the fast decaying water-column reverberations introduce high-frequency noise in the transfer function that is filtered out using the lowpass filter in the receiver function. Figure format is the same as Figure (2).

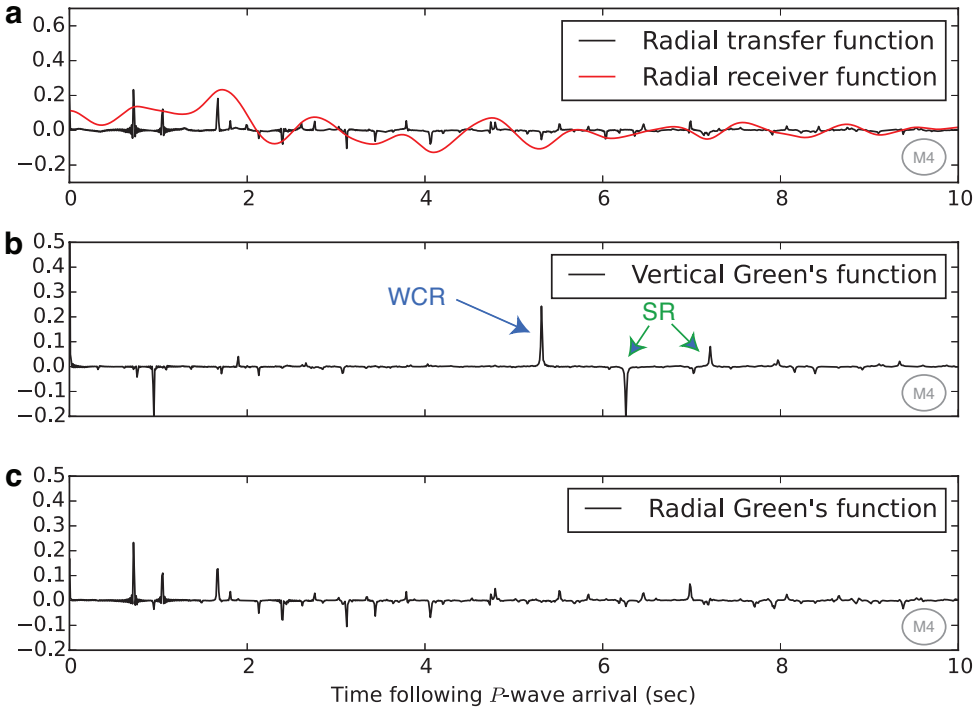

Figure 6. Results for an OBS station located at a depth of 4000 m bsl on top of a 1.2 km thick low-velocity layer of sediments (model M4, Fig. 1). The presence of the low-velocity sediments completely distorts the structural signals in the receiver function. Interpretation of receiver functions in the presence of a layer of sediments is therefore highly biased. Figure format is the same as Figure (2). SR: sediment reverberations from the pressure pulse.

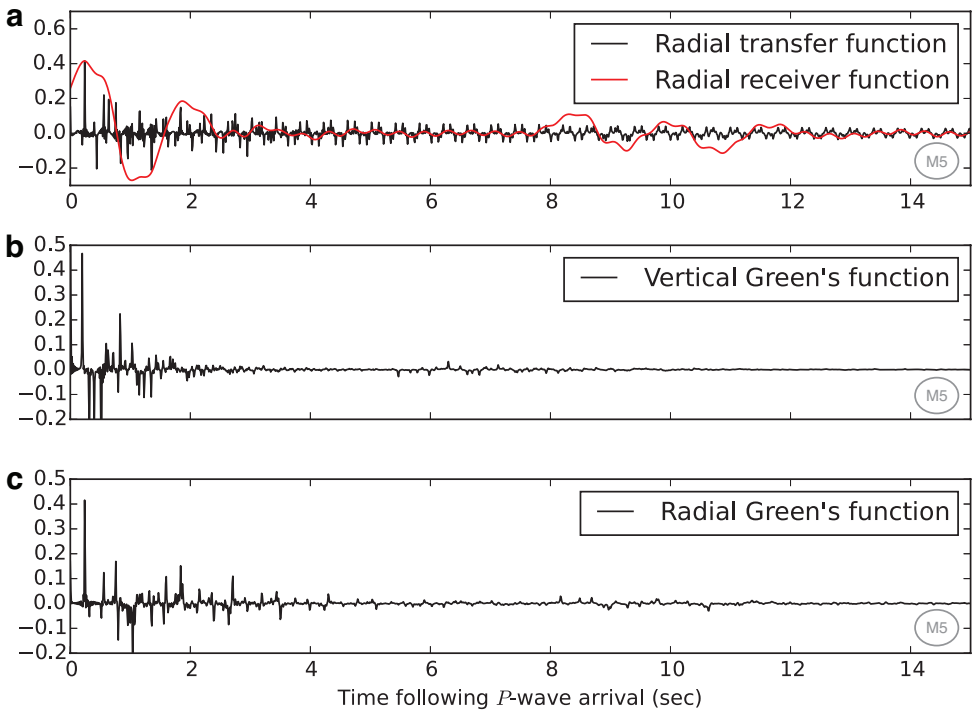

Figure 7. Results for the continental shelf model for an OBS station located at a depth of 150 m bsl on top of a 400 m thick layer of low-velocity sediments (model M5, Fig. 1). The high-frequency, erratic appearance of the Green's functions produce a highly biased and essentially useless receiver function. Figure format is the same as Figure (2).

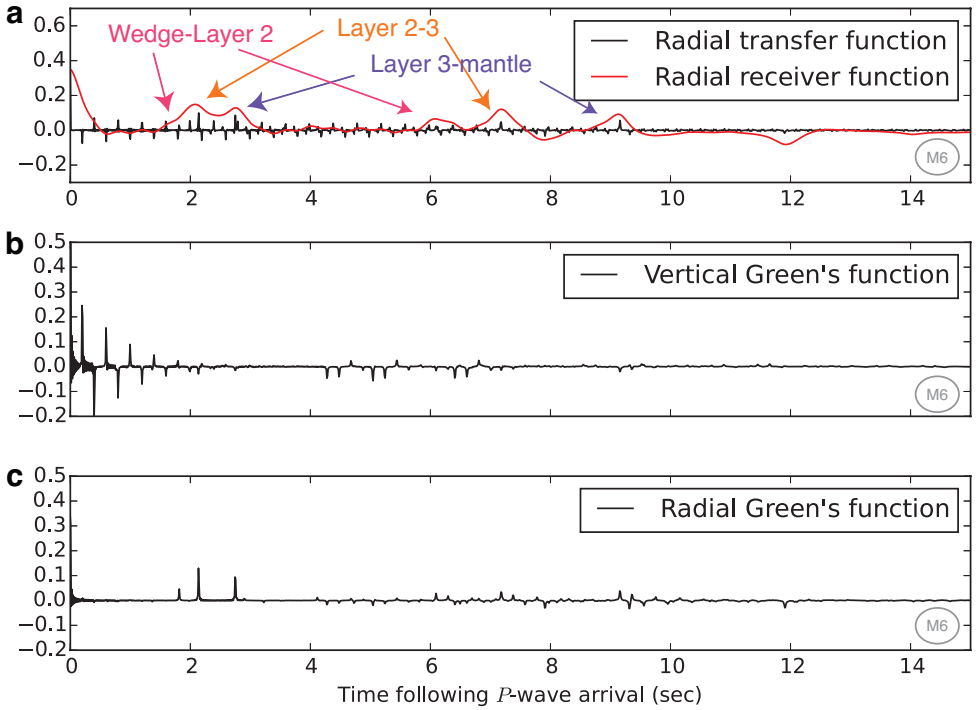

Figure 8. Results for the subduction zone forearc model with a normal oceanic crust V_P/V_S for an OBS station located at a depth of 150 m bsl (model M6, Fig. 1). Various Ps and Pps arrivals are distinguishable, all appearing as positive pulses. Figure format is the same as Figure (2).

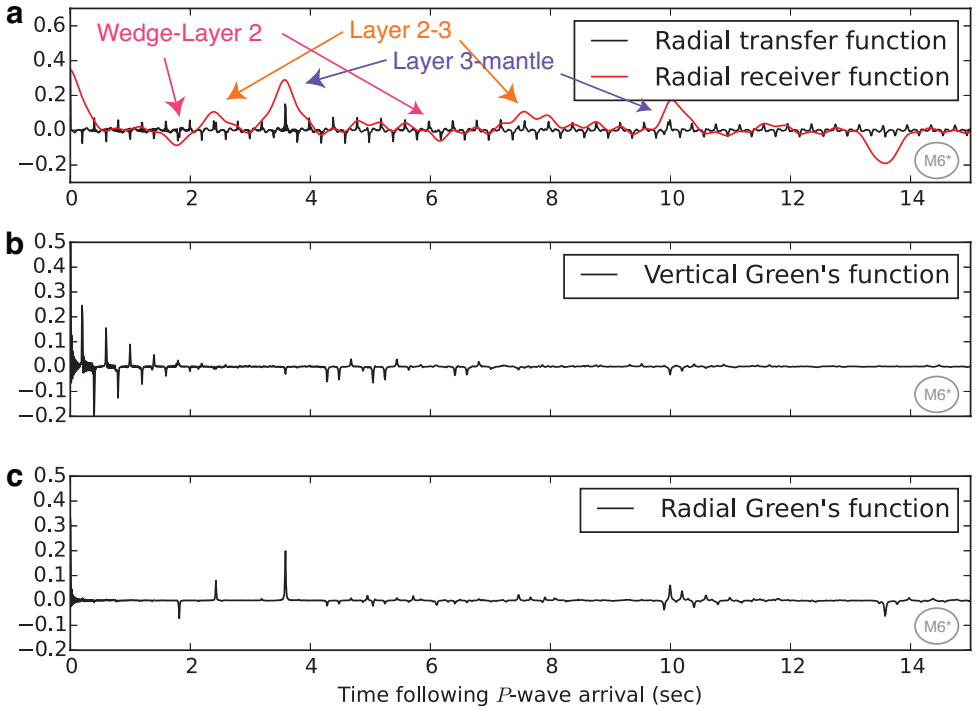

Figure 9. Results for the subduction zone forearc model with elevated V_P/V_S of 2.5 in Layer 2 for an OBS station located at a depth of 150 m bsl (model M6*, Fig. 1). In this case we see the appearance of the negative Ps pulse from the wedge-Layer 2 interface preceding the positive Ps crustal arrivals. Figure format is the same as Figure (2).

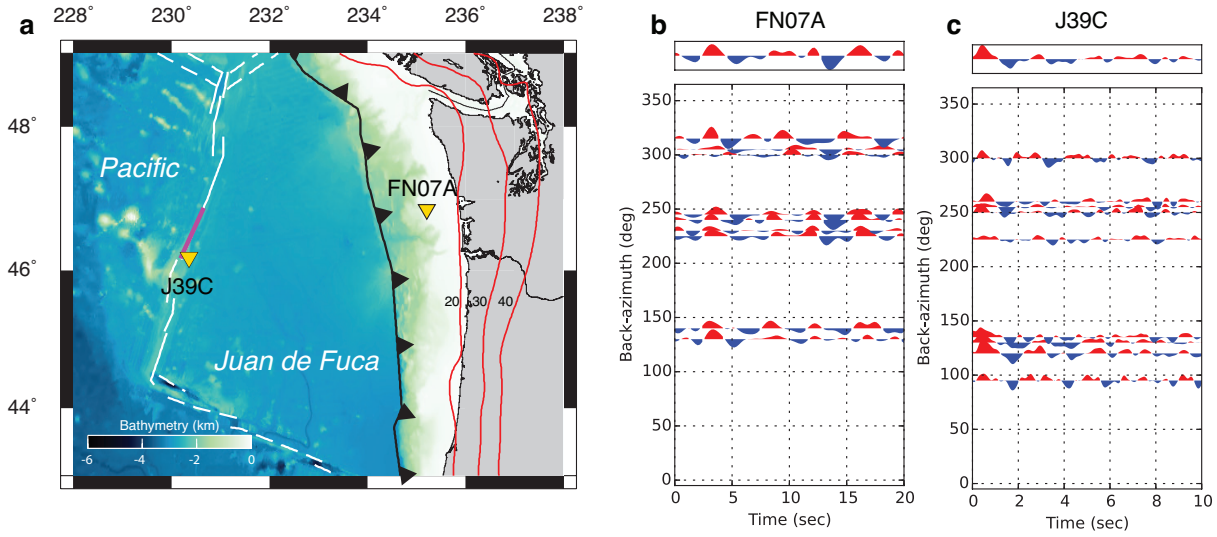

Figure 10. a, Map of the stations FN07A and J39C that are part of the Cascadia Initiative. Red lines correspond to the 20, 30 and 40 km plate interface contours from Audet et al. (2010). Solid and dashed white lines are ridge and transform plate boundaries (Bird, 2003). The magenta line shows the approximate location of the Co-Axial segment of the Juan de Fuca ridge. **b, c**, Observed radial receiver functions for stations FN07A (**b**) and J39C (**c**). Data are sorted by back-azimuth bins and stacked over all slownesses. The top traces show the stacks over all back-azimuths that include 18 events for station FN07A and 15 events for station J39C. Receiver functions are filtered between 0.1 and 0.5 Hz for station FN07A, and between 0.1 and 1.5 Hz for station J39C.

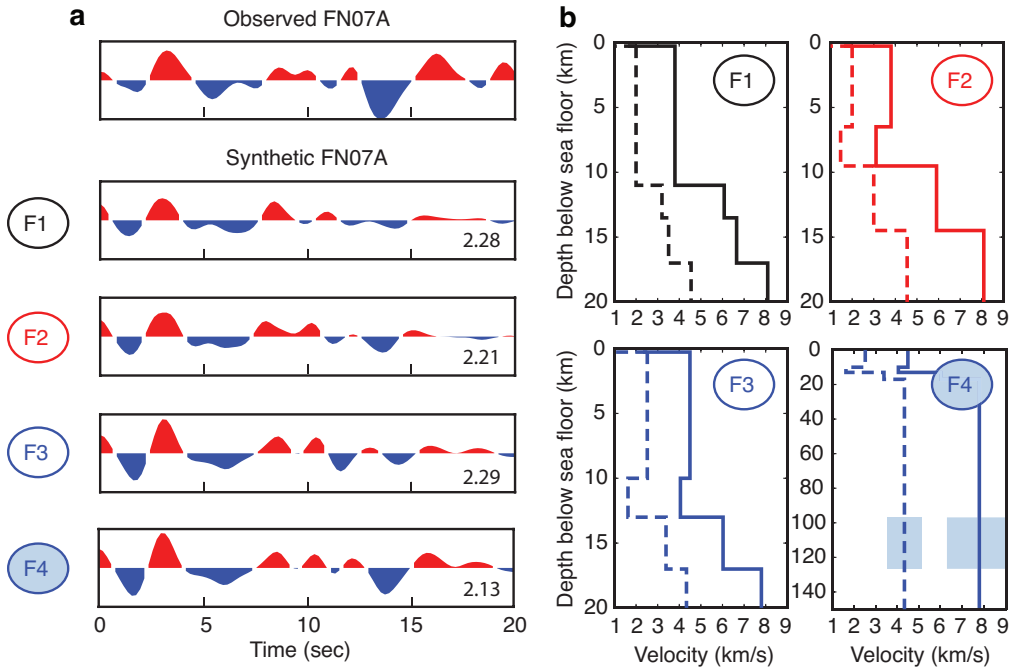

Figure 11. Comparison between observed and synthetic radial receiver function stacks (**a**) for station FN07A for various crustal velocity models (**b**). Circled labels to the left of each synthetic stack in **a** correspond to each S-wave velocity models shown in **b** and in Table 3. Numbers at the bottom right of each receiver function stack in **a** indicate the root-mean-square error between the observed and synthetic data. Solid and dashed lines correspond to P- and S-wave velocities, respectively. The models include a 150 m-thick ocean layer that is barely visible in the plots. Shaded area in model F4 (**b**) represents a layer with 30% anisotropy (see details in text). The good match between the observed and the synthetic data suggests that OBS receiver functions can provide constraints on crustal seismic properties in subduction zone settings.

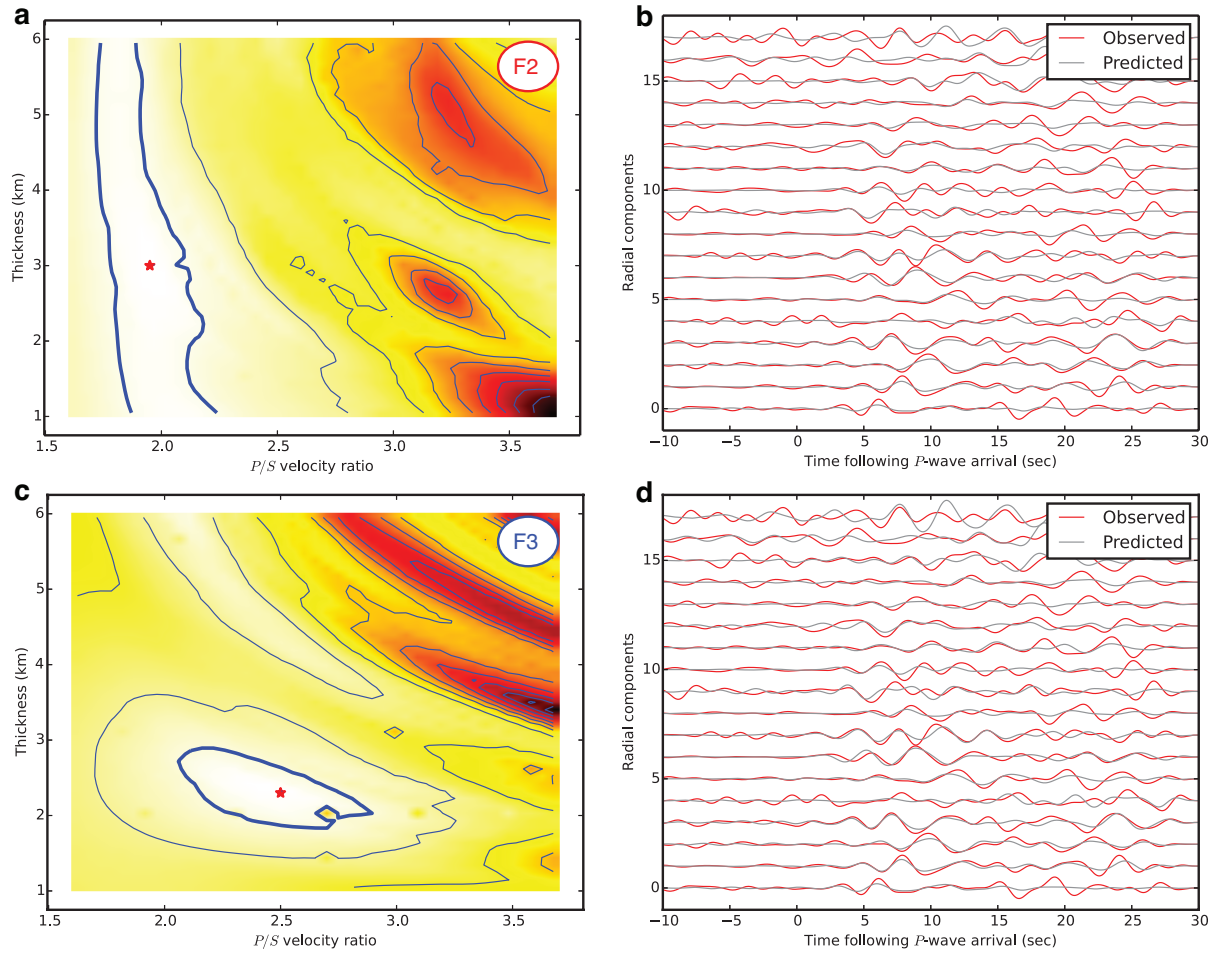

Figure 12. a, c, Grids of misfit values between predicted and observed radial components for the thickness and V_P/V_S of a low-velocity layer atop the oceanic crust for station FN07A for models F2 (**a, b**) and F3 (**c, d**) (see Fig. 11**b**). Dark colors indicate high misfit. The red star indicates the lowest misfit. The thick blue line represents the 95% confidence interval used to estimate the error on the best-fit parameters. **b, d**, Predicted (grey) and observed (red) radial component waveforms filtered between 0.1 and 0.5 Hz using the best-fit parameters obtained in **a** and **c**, respectively.

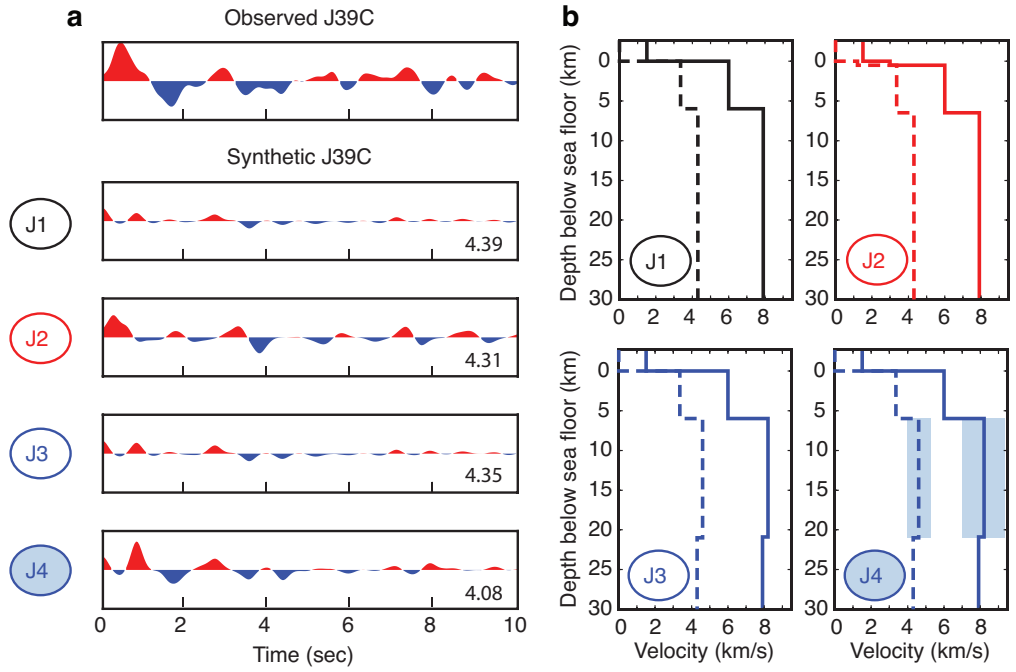

Figure 13. Comparison between observed and synthetic radial receiver function stacks (**a**) for station J39C for various crustal velocity models (**b**). Circled labels to the left of each synthetic stack in **a** correspond to each S-wave velocity models shown in **b** and in Table 4. The models include a 2650 m-thick ocean layer. Shaded area in model J4 (**b**) represent a layer with 30% anisotropy (see details in text). Figure format is the same as Figure 11.

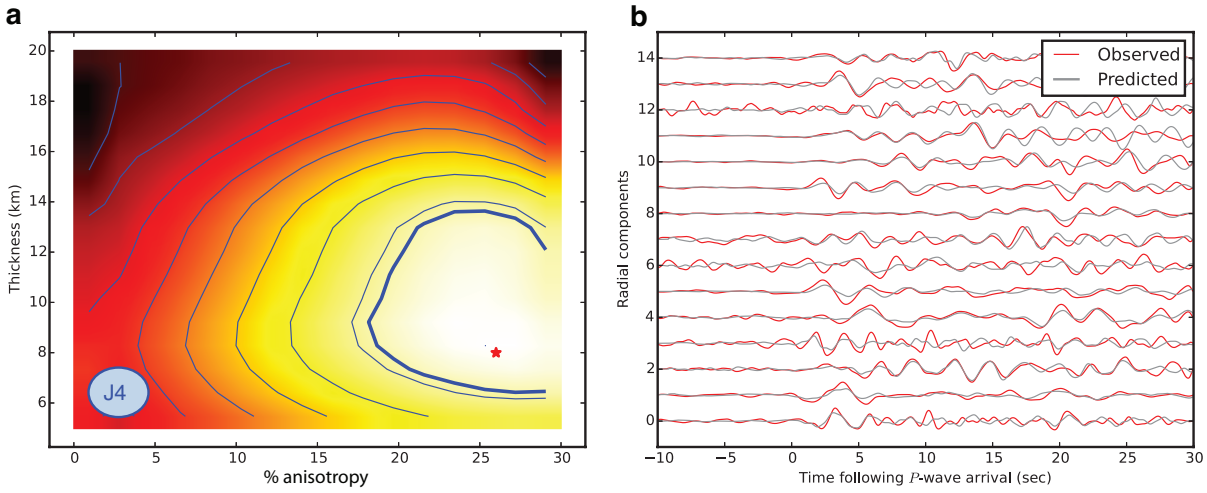

Figure 14. Grid of misfit values between predicted and observed radial components (filtered between 0.1 and 1.5 Hz) for the thickness and percent anisotropy of the oceanic mantle lid for station J39C near the Juan de Fuca Ridge (model J4, Fig. 13**b**). Figure format is the same as Figure 12.